2 Physical Principles of Dynamic Contrast-Enhanced and Dynamic Susceptibility Contrast MRI

Mark S. Shiroishi, Jerrold L. Boxerman, C. Chad Quarles, Daniel S. R. Stahl, Saulo Lacerda, Naira Muradyan, Timothy P. L. Roberts, and Meng Law

Introduction

The use of dynamic contrast-agent-enhanced magnetic resonance imaging (MRI) can provide insight into hemodynamic processes not detectable using conventional contrast-enhanced magnetic resonance (MR) techniques. This additional data may allow refinement of differential diagnoses based on microvascular physiology. The dominant dynamic gadolinium-based contrast agent (GBCA) injection MRI techniques currently utilized in brain imaging are: (1) T1-weighted dynamic contrast-enhanced (DCE) MRI, and (2) T2/T2*-weighted dynamic susceptibility contrast (DSC) MRI. Of these, DSC-MRI is much more commonly used for clinical perfusion imaging of the brain, especially for the evaluation of stroke and tumor. On the other hand, DCE-MRI is the dominant method of dynamic contrast-enhanced MRI outside of the brain [1]. In both DCE-MRI and DSC-MRI, dynamic images are acquired before, during, and after the administration of an exogenous GBCA. As opposed to other techniques, such as contrast-enhanced computed tomography (CT), contrast-enhanced MRI is distinctive because it detects the changes induced in the local relaxation times of water rather than detecting the GBCA itself, where the passage of a GBCA through tissue decreases the intrinsic T1, T2, and T2* relaxation times [2]. This chapter will provide an overview of the general physical principles of these techniques. An overview of these two methods is provided in Table 2.1 [3].

Table 2.1 Overview of DCE-MRI and DSC-MRI

	DCE-MRI	DSC-MRI
Bolus handling	Bolus passage	Bolus tracking
Acquisition point	Accumulation of contrast agent	First-pass of contrast agent
Contrast media	Intravenous bolus injection of a GBCA	Intravenous bolus injection of a GBCA
Tracer	Flow or permeability-limited diffusible tracer	Non-diffusible blood pool tracer
Relaxation mechanism	T1 relaxation	T2/T2* relaxation
Effect	T1 shortening effect	Increased susceptibility effect
Signal behaviors	Increased signal	Decreased signal

DCE-MRI dynamic contrast-enhanced magnetic resonance imaging, *DSC-MRI* dynamic susceptibility contrast magnetic resonance imaging, *GBCA* gadolinium-based contrast agent
Source: Adapted under terms of Creative Commons license from [3]

M. S. Shiroishi (✉)
Division of Neuroradiology, Department of Radiology, Keck School of Medicine of University of Southern California, Los Angeles, CA, USA
e-mail: Mark.Shiroishi@med.usc.edu

J. L. Boxerman
Diagnostic Imaging, Warren Alpert Medical School of Brown University, Providence, RI, USA

Department of Diagnostic Imaging, Rhode Island Hospital, Providence, RI, USA
e-mail: jboxerman@lifespan.org; Jerrold_Boxerman_Mdph@brown.edu

C. C. Quarles
Division of Neuroimaging Research, Barrow Neurological Institute, St. Joseph's Hospital and Medical Center, Phoenix, AZ, USA
e-mail: Chad.quarles@dignityhealth.org

D. S. R. Stahl
Rutgers New Jersey Medical School, Newark, NJ, USA

S. Lacerda
Radiologia - Neurorradiologia na Hospital da Bahia, Salvador, Bahia, Brazil

N. Muradyan
U.S. Food and Drug Administration, Center for Devices and Radiological Health, Silver Spring, MD, USA
e-mail: Naira.Muradyan@fda.hhs.gov

T. P. L. Roberts
Department of Radiology, Children's Hospital of Philadelphia, Philadelphia, PA, USA
e-mail: robertstim@email.chop.edu

M. Law
Nuclear Medicine, Neuroscience, Electrical and Computer Systems Engineering, Monash University, Alfred Health Organization, Melbourne, VIC, Australia
e-mail: meng.law@monash.edu

S. H. Faro, F. B. Mohamed (eds.), *Functional Neuroradiology*, https://doi.org/10.1007/978-3-031-10909-6_2

T1-Weighted Dynamic Contrast-Enhanced MRI

When applied to the brain, DCE-MRI is primarily employed to characterize the functional integrity of the blood–brain barrier (BBB) via estimation of microvascular permeability to GBCAs. The evaluation of cancer is a major application of DCE-MRI where it has potential to provide prognostic, predictive, and physiological response imaging biomarkers. Conventional GBCAs used in clinical MRI are diffusible, low-molecular-weight extracellular agents (~500 to 1000 Da) that remain intravascular when the BBB is intact. Disruption of the BBB secondary to a variety of pathological processes results in the transfer of GBCA moieties across the capillary endothelium from the intravascular space into the extravascular–extracellular space (EES). Leakage of GBCAs into the EES results in T1-shortening and contrast enhancement on T1-weighted imaging.

DCE-MRI Acquisition

There has historically been quite a variation of DCE-MRI acquisition protocols in the literature. DCE-MRI acquisition parameters are generally intended to emphasize R1 contrast and minimize competing T2* effects by employing short echo times (TEs) and repetition times (TRs) [2]. DCE-MRI most often utilizes a fast T1-weighted spoiled gradient-recalled echo sequence with the temporal resolution contingent on the volume coverage, contrast-to-noise ratio (CNR), and spatial resolution for a particular organ system [4, 5]. The temporal resolution demands for DCE-MRI are generally less than that for DSC-MRI unless an arterial input function (AIF) is needed [2]. DCE-MRI scan durations are generally much longer than for DSC-MRI and to estimate microvascular permeability with DCE-MRI, the temporal resolution generally ranges between 5 and 20 s [6–8]. Like with DSC-MRI, consistent technique including the use of a power injector for bolus injection (2–4 cc/s) of GBCA followed by a 20–30 cc saline flush at the same rate into the right arm to decrease possible venous reflux should be performed if possible in all cases.

Recent initiatives such as those by the Radiological Society of North America's (RSNA's) Quantitative Imaging Biomarkers Alliance (QIBA) have focused on standardizing acquisition and analysis of various imaging methods including DCE-MRI. QIBA recommendations for DCE-MRI acquisition are included in Table 2.2 [5]. (Please see section "Standardization Efforts and Variability of DCE-MRI" below). In addition to conventional DCE-MRI acquisition methods, there have been several recent advances in pulse sequence acceleration methods to obtain high temporal and/or spatial resolution in DCE-MRI. These include dynamic compressed sensing combined with parallel imaging (GRAPPA) along with two-dimensional (2D) or three-dimensional (3D) + simultaneous multislice imaging (SMS) encoding [9], radial *k*-space encoding with golden angle ordering (GRASP) method [10], high under-sampling factors, [11] and time-resolved MR angiography methods with keyhole view-sharing [12].

Table 2.2 QIBA DCE-MRI acquisition parameters for brain imaging

Parameter	DCE-MRI	
Field strength	1.5/3T	
Acquisition sequence	3D SPGR	
Receive coil type	≥8 channel head array coil	
Lipid suppression	On	
Slice thickness	≤5 mm	
Gap thickness	0–1 mm	
FOV	220–240 mm	
Acquisition matrix	256 × 128–160	
Plane orientation	Axial	
Phase/frequency encode direction	AP/RL	
Receiver bandwidth	250 Hz/pixel	
	Pre-contrast	Post-contrast
# Phases	≥5	40–80
# Averages	≥1	1
Flip angles	2–30[a]	25–30
TR (ms)	3–8 ms[b]	3–8
TE	≤3 ms[b]	≤3 ms
Temporal resolution	<10 (ideal 5) s	
Total acquisition time	5–10 min	

3D three dimensional; *DCE-MRI* dynamic contrast-enhanced magnetic resonance imaging, *FA* flip angle, *FOV* field of view, *SPGR* spoiled gradient recalled aqcquisition; *TE* echo time, *TR* repetition time
Source: Adapted with permission from [5]
[a] Variable FAs for T10 measurement
[b] Ensure that TR/TE stays constant for all FAs

DCE-MRI Data Analysis

In DCE-MRI, the concentration of GBCA must be determined in order to perform pharmacokinetic (PK) modeling. This is accomplished by measuring changes in T1-weighted signal intensity and assuming that these changes are proportional to GBCA concentration. This is a commonly used assumption given its simplicity; however, at high tracer concentrations, the relationship between signal intensity and GBCA concentration is non-linear and this can result in systematic error of DCE-MRI parameters.

Some studies have utilized predetermined T1 values, usually from the literature. However, this too can result in bias for several reasons: these are often performed in healthy subjects and there is then no consideration of the effects of aging or pathological conditions nor does it consider individual variability or tissue heterogeneity [1, 13–18]. Therefore, direct measurement of T1 in a given individual is more desirable because of potential T1 variability, particularly from pathological states. The gold standard method of

T1 mapping uses inversion recovery (IR) sequences; however, their long acquisition times preclude routine use [19]. The most commonly employed form of clinical T1 mapping is the variable flip angle (VFA) method using flip angles (FAs) of 2–30° with a gradient echo sequence (Table 2.2) [5]. The accuracy of T1 mapping relies on FA accuracy, which can be compromised due to several factors including the presence of standing waves from dielectric resonance in a subject [20], less uniform FA from smaller transmit coils, and poor slice profiles from 2D multi-slice imaging [21]. B1 mapping can be particularly helpful to correct FA inaccuracies, particularly at 3T and over large anatomic coverage [5, 22]. In addition to the IR and VFA methods, the Look-Locker (LL) method is another technique for T1 mapping. Like the VFA method, LL methods are faster than IR; however, they may also result in errors with studies suggesting that VFA may result in overestimation while LL may underestimate T1 values due to inaccurate B1 mapping and incomplete spoiling [19].

The determination of the arterial input function (AIF) to obtain more accurate measurement of the concentration of GBCA in blood plasma ($C_p(t)$) can be another source of error in DCE-MRI. Partial-volume average artifacts due to limitations in spatial resolution can result from the sampling of a small cerebral artery. Sampling from a large vein such as the superior sagittal sinus as a venous outflow function (VOF) can be used to correct partial-volume average artifacts by rescaling the area under the AIF curve [23–25]. The use of three-dimensional (3D) image acquisition, ensuring that the artery of interest is well visualized in the excitation slab, or using non-selective saturation pre-pulse can help alleviate inflow artifacts where the arterial blood appears bright on pre-contrast images [26]. If measurement of an individual AIF is not practical, other alternatives that have been used include population-based AIFs that do not incorporate individual differences. There are also reference tissue models that attempt to estimate the vascular tracer concentration from one or more normal-appearing surrounding tissues [27]. Hematocrit values should theoretically be incorporated into the AIF measurement because the GBCA remains in the blood plasma component and does not pass into red blood cells. However, in practice, a standard, rather than a directly measured, hematocrit value is used and this too can result in errors [4].

There are a variety of methods to analyze DCE-MRI data. At its most basic, non-PK modeling methods use subjective assessment of the signal intensity-time curve. These are simple to perform and interpret, yet will not provide in-depth understanding of the underlying pathophysiology [28]. Other methods involve semi-quantitative analysis of data with metrics such as the initial area under the enhancement curve (IAUC) and other methods of signal intensity-time curve analysis that provide more detailed characterization of the kinetics of GBCA tissue accumulation [28, 29]. While easier to perform than PK modeling of DCE-MRI data, these semi-quantitative methods cannot distinguish between physiologic factors and physical properties of image acquisition including, but not limited to, scanner parameters, method of GBCA administration, and native T1 of the interrogated tissue [30–32].

DCE Pharmacokinetic Modeling

Through more sophisticated PK modeling of DCE-MRI data, various quantitative parameters can be determined: the volume transfer constant between blood plasma and the EES (K^{trans}), the volume of EES per unit volume of tissue (v_e), the rate constant between EES and blood plasma (k_{ep}, where $k_{ep} = K^{trans}/v_e$), capillary wall permeability surface area product per unit volume of tissue ($PS\rho$), and capillary blood flow (perfusion) per unit volume of tissue ($F\rho$) [6]. Most DCE-MRI tracer kinetic models divide the tissue of interest into several compartments (Fig. 2.1). These include the blood plasma volume per unit volume of tissue (v_p) and the volume of extravascular–extracellular space per unit volume of tissue (v_e).

Of the various PK models that have been used to analyze DCE-MRI data, the most popular model is commonly referred to as the Tofts model [6, 33] and provides measures of K^{trans} and v_e. K^{trans} was originally described by the following equation:

$$v_e \frac{dC_e(t)}{dt} = K^{trans}\left(C_p(t) - C_e(t)\right)$$

where C_p and C_e are the blood plasma and EES contrast agent concentrations, respectively (Fig. 2.1). K^{trans} is the most frequently utilized metric in DCE-MRI and describes the rate of contrast agent flux into the EES. Its physiological meaning

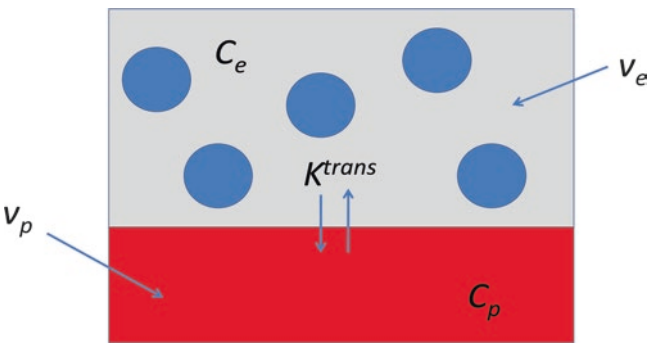

Fig. 2.1 Schematic of two-compartment model in DCE-MRI. Keys: v_p = blood plasma volume per unit volume of tissue; v_e = volume of extravascular extracellular space per unit volume of tissue; K^{trans} = volume transfer constant between blood plasma and EES; C_p = tracer concentration in arterial blood plasma; C_e = tracer concentration in EES; and blue circles = intracellular space where contrast agent is excluded

can be complex as it is dependent on vascular permeability, capillary surface area, and the type of contrast agent utilized [34]. When there is very high permeability of the endothelium with respect to blood flow, ($F << PS$), K^{trans} primarily reflects blood flow—($K^{trans} = F(1 - Hct)$—as this is the main limiting factor of the contrast agent flux; in this case, DCE-MRI could be seen as "perfusion imaging." When there is very low permeability as compared to blood flow ($F >> PS$), K^{trans} mainly reflects permeability ($K^{trans} = PS$), and in these situations DCE-MRI could be referred to as "permeability imaging" [6, 34, 35].

In the original Tofts model, neglecting the contribution of intravascular tracer to the MRI signal may be appropriate for a diffusible tracer where its distribution volume is large relative to blood volume. However, with an extracellular tracer, this may be problematic as its distribution volume is smaller [6, 36]. This assumption may produce erroneous K^{trans} estimates because intravascular tracer could contribute a significant proportion of the observed tissue signal. Therefore, in the presence of an intravascular–extracellular tracer, the model has been modified and expressed as:

$$C_t(t) = v_p C_p(t) + K^{trans} \int_0^t C_p(\tau) e^{-K^{trans}(t-\tau)/v_e} d\tau$$

where v_p represents the blood plasma volume per unit volume of tissue. This model is often referred to as the "extended Tofts model" [6] (Fig. 2.1). v_p may be ignored in situations when the plasma volume or tracer concentration is negligible; e.g., hypovascular low-enhancing tissues or a few minutes after the bolus. However, in diseases that are highly perfused, such as neoplasms, there should be consideration of v_p [4] (Fig. 2.2).

There are less commonly utilized PK models besides the Tofts and extended Tofts models. While the Tofts models assume a bi-directional exchange of CA between the vascular space and EES, a simpler assumption of a unidirectional transport of CA from the vascular to the EES compartment can be formulated. The "Patlak model" [37] utilizes this form and can be expressed as:

$$C_t(t) = v_p C_p(t) + K^{trans} \int_0^t C_p(\tau) d\tau$$

The two-compartment exchange model (2XCM) is a more generalized kinetic model than the Tofts and Patlak models. It can be used in mixed perfusion and permeability conditions that can allow estimation of PS and F to be calculated [1, 38, 39]. This takes the form of:

$$v_p \frac{dC_p(t)}{dt} = F(C_a - C_p) - K_{PS}(C_p - C_e) \text{ and } v_e \frac{dC_e(t)}{dt} = K_{PS}(C_p - C_e)$$

where C_a represents the AIF and K_{PS} now can be thought of as K^{trans} without the F versus PS uncertainty. It is important to note that more complex modeling such as this necessitates increased concern regarding sources of error during data acquisition and analysis [40, 41].

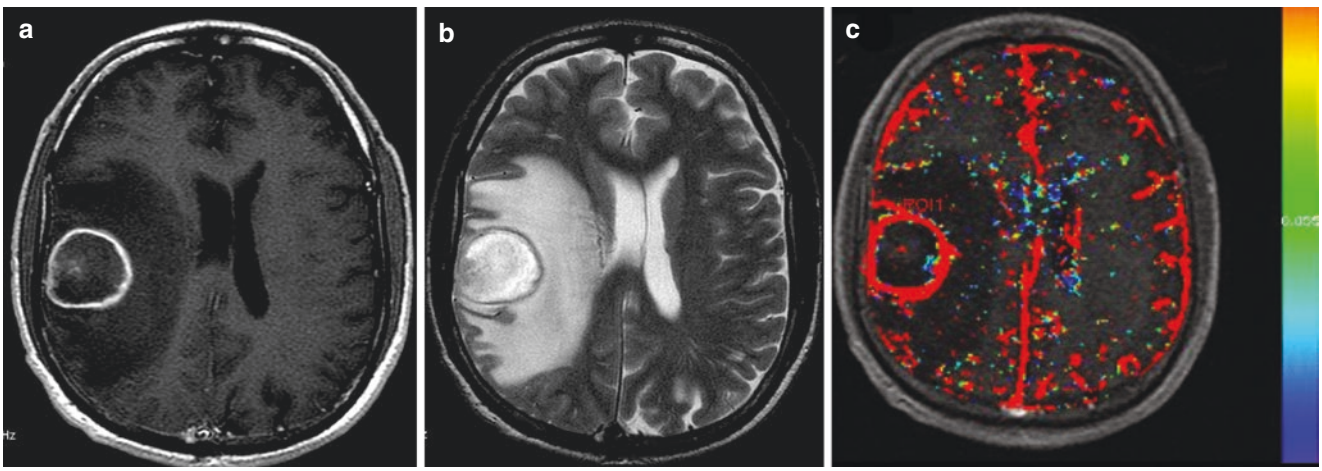

Fig. 2.2 A 52-year-old female with pathology-proven high-grade glioma. (**a**) Axial contrast-enhanced T1-weighted image and (**b**) axial T2-weighted image demonstrate an enhancing tumor in the medial aspect of the right temporal lobe. (**c**) K^{trans} color map demonstrating a lesion with high values in the enhancing wall of the tumor

Standardization Efforts and Variability of DCE-MRI

Lately, there has been increasing awareness regarding the need to decrease bias and variability of quantitative imaging biomarkers. Efforts such as the RSNA's QIBA have focused on various imaging methods including DCE-MRI [42]. The QIBA Perfusion Biomarker Committee Task Force has been continuously working on their DCE-MRI profile [43]. The goal of QIBA profiles such as the one on DCE-MRI is to assist in achieving adequate performance for an imaging biomarker and to provide details about the capabilities and limitations of an imaging marker. It does so by offering guidance regarding imaging acquisition, devices, technologists, radiologists, subject handling, image quality assurance, reconstruction software, imaging analysis tools, and image quality assurance.

Standardization of image acquisition parameters is a major point of emphasis for QIBA. Inter-scanner and inter-site variability of T1 values in the brain is well known where the Look-Locker IR method can underestimate while the VFA technique can overestimate white matter T1 measurements [19]. Factors such as the particular MR sequence employed, B_1 field inhomogeneity, temperature of the magnet bore, and incomplete spoiling of transverse magnetization can influence the derived T1 values [44]. Before the acquisition of clinical DCE-MRI data, it is important to determine the true scanner variance and bias for T1 values through the use of a T1 phantom. The QIBA DCE-MRI T1 phantom is composed of spheres containing solutions of varying concentrations of nickel chloride [44]. The phantom contains two sets of spheres: one set to simulate the vascular input function and the other set to represent tissue (Fig. 2.3). The T1 values for the vascular input spheres range between 0.75 and 41.6 s^{-1} while the tissue spheres range between 0.67 and 7.5 s^{-1}. The phantom is filled with 30-mM sodium chloride solution to simulate patient coil loading. To obtain T1 values, an acquisition protocol that encompasses the typical VFAs is used for T1 mapping. This employs a coronal fast spoiled gradient echo sequence with VFAs of 2, 5, 10, 15, 20, 25, and 30°. The use of the QIBA DCE phantom to determine test–retest reliability and T1 accuracy is particularly important in longitudinal DCE-MRI studies. In order to analyze image data from the QIBA DCE-MRI phantom, QIBA also provides automated T1 quantification software [45].

A recent multicenter phantom study of vendor-provided B1 mapping sequences demonstrated the potential for these techniques to provide unbiased and reproducible quantification of B1 field inhomogeneity that could be used to account for spatial variation in the transmitted radio frequency (RF) field [46]. Version 2.0 of the RSNA QIBA DCE-MRI Profile is currently being written and it will address spatially dependent B1 field inhomogeneity effects that may affect VFA T1 measurements. This is particularly problematic at higher fields like 3T and when data are acquired over large anatomic regions and may necessitate B1 mapping and corrections to be incorporated in the measurement of T1 values [5].

While the QIBA T1 phantom is a static phantom, there has been recent work by Kim et al. [47] on a dynamic perfusion phantom focused on DCE-MRI of the abdomen. They used two different 3T MRI scanners and three healthy volunteers. When compared to a static phantom, they found that the perfusion phantom significantly decreased the variability of contrast concentration and K^{trans} measurements measured in four abdominal organs (liver, spleen, pancreas, and paravertebral muscles). One should note that while estimates of DCE-MRI performance can be conducted with phantoms, these experiments likely underestimate the variability produced in clinical populations due to the absence of motion artifacts [5].

Few clinical DCE-MRI studies of variability have been done in the brain and more data are desperately needed. However, practical difficulties centering on the need to do multiple GBCA injections in patients make such studies difficult to conduct. One such study was performed in 2003 by Jackson et al. [48] in 9 glioma patients and found that the within-region of interest (ROI) coefficient of variation for mean K^{trans} was 7.7% with a repeatability coefficient of 21.3%. A more recent publication by Barboriak et al. in 2019 [49] found that in a multicenter imaging study of recurrent glioblastoma, less variation in inter-reader tumor segmentation volumes, possibly through the use of automated tools, may decrease variability in DCE-MRI metrics like K^{trans}.

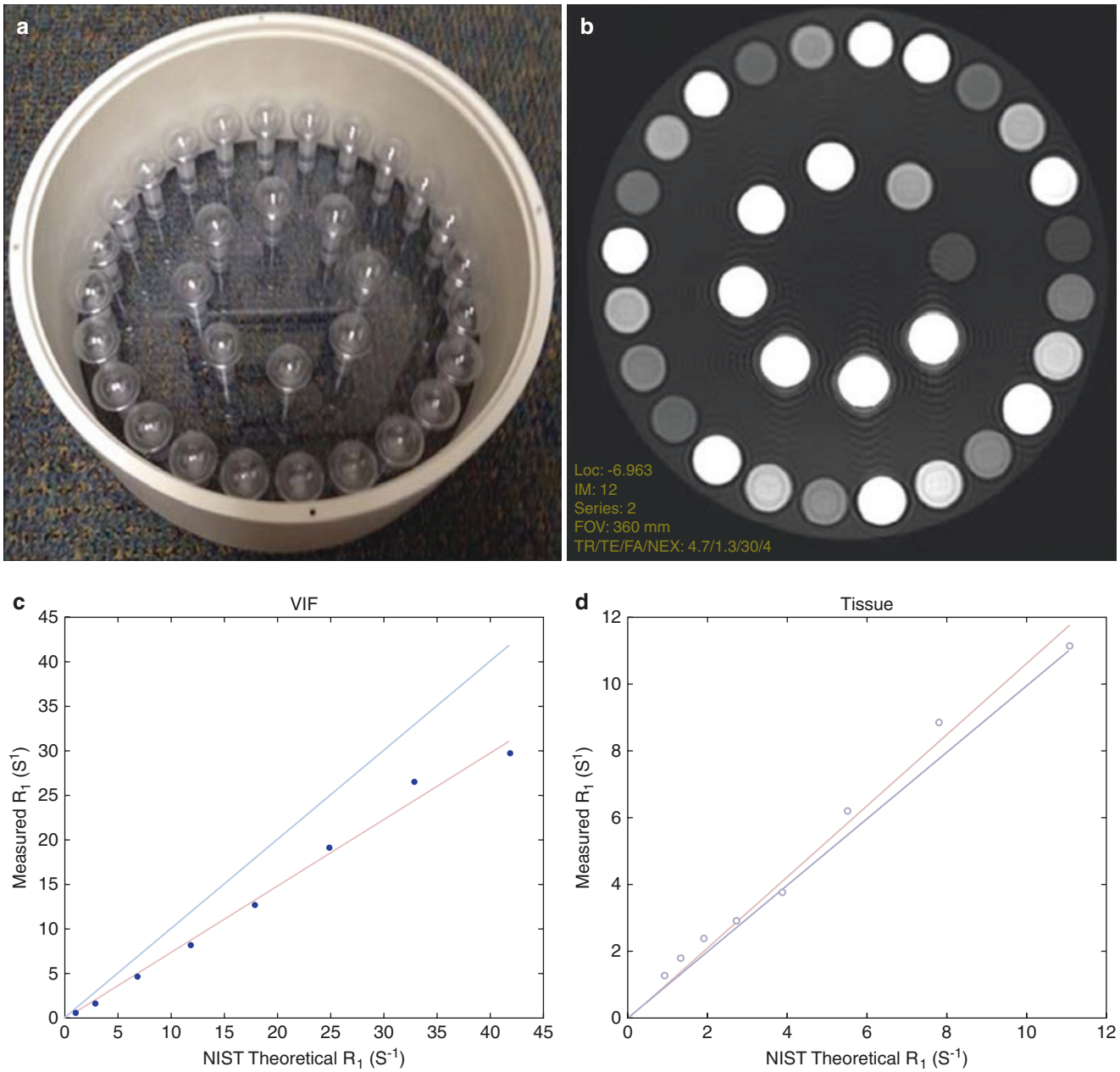

Fig. 2.3 (**a**) The QIBA dynamic contrast-enhanced phantom layout with 32 spheres, with different concentrations of $NiCl_2$ solutions for varying T1 relaxation rates (R1). (**b**) T1-weighted MR image of the phantom showing the 32 spheres and (**c**) R1 values of the eight-vascular input function-mimicking inserts compared with National Institute of Standards and Technology (NIST) theoretical R1 values. (**d**) R1 values for the 24 tissue-mimicking inserts. (Images contributed by Edward Jackson, University of Wisconsin-Madison. Reprinted with permission from [5]

T2/T2*-Weighted Dynamic Susceptibility Contrast MRI

Dynamic susceptibility contrast (DSC)-MRI has been applied to many neurological diseases, most prominently brain tumors and stroke. Compared to DCE-MRI, DSC-MRI is much more commonly used in the clinical setting for brain imaging, though the opposite is true outside of the brain. Also sometimes referred to as bolus tracking MRI, a non-diffusible tracer, typically a GBCA, is administered and rapid images are obtained during the first-pass of the contrast agent. Several parameters are derived from DSC-MRI including relative cerebral blood flow (CBF), mean transit time (MTT), and relative cerebral blood volume (rCBV). rCBV is generally considered the most widely utilized and robust DSC-MRI perfusion metric in brain imaging.

DSC-MRI Acquisition

Like DCE-MRI, DSC-MRI acquisition consists of images acquired before, during, and after administration of an intravascular contrast administration (CA). While DCE-MRI emphasizes T1 contrast and uses short TE and TR to minimize competing T2* effects, DSC-MRI emphasizes T2* and T2 contrast. Accordingly, long TE and TR are used to minimize competing T1 effects [2]. In gradient echo-echo planar imaging (GRE-EPI DSC-MRI), TE is usually in the range of 25–35 ms in order to optimize T2* weighting, signal-to-noise ratio (SNR), and sensitivity to T1 effects [2, 50, 51]. With regard to TR, 1.5 s or less is recommended to optimize temporal resolution given the constraints of desired slices, TE and T1 weighting [2, 50, 51]. Regardless of whether GRE or spin echo (SE) sequences are used, DSC-MRI requires very robust temporal resolution (<2 s/time point) with adequate spatial resolution. Given the need for high temporal resolution, single-shot EPI sequences are typically used. Some newer methods designed to address the image distortion and signal dropout artifacts that degrade traditional EPI acquisitions include single-line acquisitions [27], spiral or radial acquisitions [52, 53], and advanced EPI readouts [54, 55].

A flip angle of 60–70° may in principle provide a compromise between SNR and T1 sensitivity from GBCA leakage effects [2, 50, 51]. Higher flip angles would result in greater SNR, but would be more susceptible to GBCA leakage effects due to increased T1 sensitivity. On the other hand, lower flip angles are less prone to GBCA leakage effects but at the cost of lower SNR. In order to avoid partial-volume average artifacts, adequate spatial resolution of 1–3 mm in plane and 3–5 mm through plane are recommended, though this may depend on desired temporal resolution [2].

Most DSC-MRI data are acquired using GRE-EPI sequences, although some have used SE-EPI. SE methods are most sensitive to smaller vessels (<20 μ[mu]m; i.e., capillaries) [56], and also are less prone to artifacts at bone–brain–air interfaces or at the skull base compared to GRE methods [57, 58]. GRE-EPI methods result in greater signal loss [2], and are sensitive to vessels of all sizes [56] with excellent signal-to-noise ratios. GRE methods also allow higher temporal resolution due to shorter TEs and this improves AIF quantification [2]. Given its sensitivity to vessels of all sizes, perfusion metrics derived from GRE could suffer from large vessel blooming artifact because of a tendency of the signal from capillaries to be dominated by macrovascular signal [59, 60]. Thus, GRE-based acquisition could provide overestimates of perfusion metrics, while SE techniques likely provide truer estimates of capillary-level perfusion compared to positron emission tomography (PET).

Newer multi-echo DSC-MRI acquisitions such as spin and gradient echo (SAGE) [61–65] allow simultaneous acquisition of GRE and SE data without adding additional scan time or GBCA injections. These methods may provide important additional complementary information given their different sensitivities to vessel size, and enable vessel size imaging (VSI) to be performed and also provide simultaneous DCE-MRI metrics with only a single dose of contrast agent. Other techniques such as spiral perfusion imaging with consecutive echoes (SPICE) methods [53] can also provide both DSC-MRI and DCE-MRI metrics in a single acquisition and without the need of a preload dose of GBCA.

The scan duration of DSC-MRI is much shorter than DCE-MRI and is shortest for indications like brain tumor evaluation (at least 2 min recommended). For other indications where there will be bolus dispersion and delay, like stroke evaluation, longer scan duration is needed [66]. DSC-MRI acquisitions are limited by compromises in spatiotemporal resolution, volume coverage, and SNR. Recent advances to accelerate DSC-MRI acquisition and achieve optimal spatiotemporal resolution include the use of parallel imaging methods [55, 67] to decrease the EPI readouts, reduce EPI-related artifacts, and decrease partial-volume effects. Other methods such as simultaneous multi-slice acquisitions [68] can accelerate DSC-MRI acquisitions by applying simultaneously exciting multiple slice planes with radiofrequency pulses without significant loss of SNR while achieving high spatiotemporal resolution.

Compared to DCE-MRI, GBCA injection rates should be relatively higher (at least 4 cc/s) for DSC-MRI in order to avoid underestimation of DSC-MRI metrics from slower rates [69]. Similar to DCE-MRI, injection should ideally be given via the right arm in order to avoid venous reflux. Approximately 60 s of baseline data should be acquired prior to the injection of a GBCA in order to provide good CBV map CNR [51]. An overview of DSC-MRI recommended acquisition parameters is given in Table 2.3 [51, 70, 71].

DSC-MRI Data Analysis

Based on the indicator dilution methods for non-diffusible tracers, CBV is proportional to the area under the contrast agent concentration (Δ[Delta]R_2* [or Δ{Delta}R_2])-time curve, assuming that there is no contrast agent leakage or recirculation [72]. While in DCE-MRI, dipole–dipole interactions are primarily responsible for GBCA-based T1 relaxation enhancement, the main contrast mechanism in DSC-MRI is susceptibility effects induced by GBCAs [73]. When a GBCA is given as a bolus, a transient drop in signal intensity is seen on the signal intensity-time curve, known as "negative enhancement," as opposed to the "positive enhancement" due to enhanced T1 relaxation in DCE-MRI or conventional contrast-enhanced T1-weighted imaging.

Table 2.3 DSC-MRI acquisition parameters for brain imaging

Parameter	DSC-MRI
Field strength	1.5/3T
Acquisition sequence	Generally GRE-EPI rather than SE-EPI
Slice thickness	3–5 mm
FOV	200 × 200 mm (range, 200 × 200 to 240 × 240 mm)
Acquisition matrix	128 × 128 (range, 64 × 64 to 256 × 256)
GBCA injection rate	At least 4 mL/s
TR	1.0–1.5 s (SE-EPI); minimum (vs "as short as possible") for GRE-EPI; generally 1.0–1.5 s
TE	45 ms at 1.5T/30 ms at 3 T
Flip angle	60°, newer consensus protocol suggests 30° with no-preload GBCA may perform as well as 60° with single-dose preload at 3 T
Temporal coverage	120 time points
Preload GBCA dose (particularly for studies performed with a high flip angle)	Single dose (0.1 mmol/kg Gd), given 5–10 min prior to dynamic imaging
Baseline acquisitions prior to GBCA injection	At least 30–50
Total acquisition time	At least 2 min (brain tumors)

DSC-MRI dynamic susceptibility contrast magnetic resonance imaging, *GBCA* gadolinium-based contrast agent, *GRE-EPI* gradient echo-echo planar imaging, *FOV* field of view, *SE-EPI* spin echo-echo planar imaging, *TE* echo time, *TR* repetition time
Source: Adapted with permission from [51, 70, 71]

Like in DCE-MRI, changes in DSC-MRI signal intensity are converted to the tissue concentration of GBCA at time t ($C(t)$). For DSC-MRI, this relation is noted on a voxel-wise basis as:

$$C(t) \propto k \cdot \Delta R_2^*(t) = -\frac{k}{\mathrm{TE}} \ln\left(\frac{S(t)}{S_0}\right)$$

where k represents a proportionality constant (often set to unity as it is not known a priori) that is dependent on tissue type, field strength, contrast agent, and pulse sequence; $\Delta R_2^*(t)$ represents the change in the T2* relaxation rate at time t; TE is the echo time; $S(t)$ represents the signal intensity at time t; and S_0 represents the baseline signal intensity before arrival of the GBCA. It is assumed that T1 effects due to an intact BBB are not significant during DSC-MRI acquisition and that there is a linear relationship between $\Delta R_2^*(t)$ and $C(t)$ [74]. However, in lesions such as brain tumors, disruption of the BBB is common and necessitates changes in acquisition and post-processing methods in order to compensate for GBCA leakage effects (discussed below). Furthermore, the assumed linear relationship between $\Delta R_2^*(t)$ and $C(t)$ may not hold true [75] and assumption of a quadratic relationship could be assumed to mitigate CBF errors, particularly when estimating the AIF [76].

The area beneath the concentration-time curve is calculated to derive the CBV map. By applying tracer kinetic modeling for intravascular tracer agents [77–80], CBV can be obtained by integrating $C(t)$ using the following relationship:

$$\mathrm{CBV} = \frac{H_f \int_0^t C_t(t)\,dt}{\rho \int_0^t C_a(t)\,dt}$$

where H_f represents the difference in hematocrit between the AIF and capillaries, $C_t(t)$ represents the concentration of GBCA in the tissues, ρ represents the brain tissue density, and $C_a(t)$ represents the AIF. The AIF can be ignored because of constraints in quantification due to limited temporal and spatial resolution and so "relative" CBV is commonly reported.

Indicator dilution theory can be used to model $C_t(t)$ using the following equation:

$$C_t(t) = CBF \cdot C_a(t) \otimes R(t) = CBF \cdot \int_0^t C_a(t) R(t-\tau)\,d\tau$$

where $\otimes$ represents convolution of $C_a(t)$ and the tissue residue function $R(t)$, which represents the amount of contrast agent that remains in the tissue at time t.

The deconvolution of the $C_a(t)$ and $C_t(t)$ is needed to quantify CBF. Of the various methods available, the most commonly used model-independent method is singular value decomposition (SVD) [81] that is expressed as:

$$C_t(t) = CBF \cdot \int_0^t C_a(t) R(t-\tau)\,d\tau \approx \Delta t \sum_{i=0}^{j} C_a(t_i) R(t_j - t_i)$$

where it is assumed that $R(t)$ and $C_a(t)$ remain constant over small time intervals and that cerebral and arterial concentrations are measured at equally spaced time points. In order for SVD to determine $R(t)$, methods have been devised to decrease errors from the potential delay between the AIF and tissue concentration curves [82] and to avoid physiologically unreasonable results due to noise that lead to unstable solutions. The most common ways to address these two issues are to implement a block-circulant AIF discretization matrix with a truncated SVD regularization approach, respectively [2].

Application of the central volume theorem allows calculation of the mean transit time (MTT):

$$\mathrm{MTT} = \frac{\mathrm{CBV}}{\mathrm{CBF}}$$

Aside from CBV, CBF, and MTT, there are several other emerging DSC-MRI parameters on the horizon. Newer kinetic models can provide estimates of oxygen extraction fraction (OEF) and capillary transit time heterogeneity (CTH) that may better relate to the oxygen delivery that could be attained for a given CBF [83]. Traditional determination of oxygen availability in the brain is determined using CBF and arterial oxygen concentration, but these newer methods have the potential to highlight perfusion derangements in brain tissue that may not be detected with conventional DSC-MRI analysis. As was mentioned previously, the use of gradient-echo and spin-echo sequences to provide simultaneous estimations of $\Delta(\text{Delta})R_2$ and $\Delta(\text{Delta})R_2^*$ can provide other parameters including measures of vessel size imaging (VSI), microvascular density, mean vessel diameter [84], and vessel architectural imaging (VAI) (Fig. 2.4) [85]. In current practice, these measures are obtained with tissue sampling and defined by the pathologist. However, validation of these techniques could overcome the limitations of sampling error and inability to perform longitudinal analysis, and may become important with the continued development of anti-vascular and anti-angiogenic therapies [86].

Arterial Input Function

Determination of the AIF is one of the leading sources of error in the quantification of DSC-MRI. Various manual and automatic approaches [87–94] have been proposed to measure the AIF, but the most commonly used approach is to use a global, as opposed to local, measurement using voxels either in or adjacent to the middle cerebral artery (MCA). While straightforward to do, assuming a global AIF will not likely be the true arterial input to the region of interest and may introduce errors in quantification due to AIF delay and dispersion [66, 95]. Delay effects can be compensated for by using AIF discretization techniques that are resistant to delay in SVD for example, while dispersion effects are difficult to adjust for when using a global AIF [2]. In stroke cases, multiple regional AIFs may diminish some of the dispersion errors [96] from vascular disease and using these along with newer models based on vascular morphology and fluid dynamics [97, 98] holds promise to combat dispersion effects.

Absolute Quantification

Absolute quantification of DSC-MRI is difficult due to several factors such as uncertainties relating to hematocrit, brain proton density constants, contrast agent relaxivity, contrast agent leakage correction, and AIF considerations [2, 50, 51]. As a result, most DSC-MRI studies rely on qualitative or semi-quantitative measures. Most often, a summary statistic in the form of "relative" CBV (rCBV) or CBF (rCBF) is often used without definition of the AIF [50]. It should be noted that in addition to "relative" CBV (or CBF), "rCBV" can also refer to "regional" CBV [99]. It is also common for relative CBV to refer to a value that is normalized to "normal" tissue, typically contralateral white matter [100], while "regional" CBV often refers to absolute quantification of CBV.

Scaling metrics such as normalization or standardization are commonly applied to non-quantitative rCBV values in order to compare between subjects and imaging sessions. However, the amount of variability intrinsic to these techniques is unclear [101]. With normalization, the mean value of the voxels within a tumoral ROI is divided by those in a reference ROI, usually that in normal-appearing white matter. Normalization is quite commonly used; however, it can be time consuming and lead to user-dependent subjectivity [102]. On the other hand, when standardization is used, there is no need to use a reference ROI because rCBV maps are transformed to a standardized intensity scale. In this way, it can function as an objective technique of converting rCBV values to a consistent scale and it appears to improve rCBV measurement consistency across patients and time [102].

Leakage Effects of GBCAs

GBCA leakage can diminish the accuracy and precision of rCBV derived from DSC-MRI. With an intact BBB, compartmentalization of GBCA within the vasculature mainly impacts T2 or T2* with minimal impact on T1, and diminutive $\Delta(\text{Delta})R^1$ is a major assumption in DSC-MRI [56]. In theory, the equation for $\Delta(\text{Delta})R_2^*$ is valid only if the changes in T1 associated with GBCA leakage do not significantly affect signal intensity. However, this assumption often does not hold true as a disrupted blood–brain barrier leading to contrast-enhancement is commonly seen in clinical practice, particularly with many brain tumors. In cases of contrast agent leakage, underestimation of rCBV may occur because GBCA leakage can diminish the magnitude of the susceptibility contrast signal intensity loss in regions where T1 effects are prominent (Fig. 2.5). At the same time, it is possible to overestimate rCBV in the face of prominent T2/T2* effects because this will result in greater signal decrease and undershooting of the baseline signal intensity. The amount of under- or overestimation of rCBV is contingent upon contrast agent kinetics, brain tissue microstructure, pulse sequence parameters, and preload GBCA dose [2].

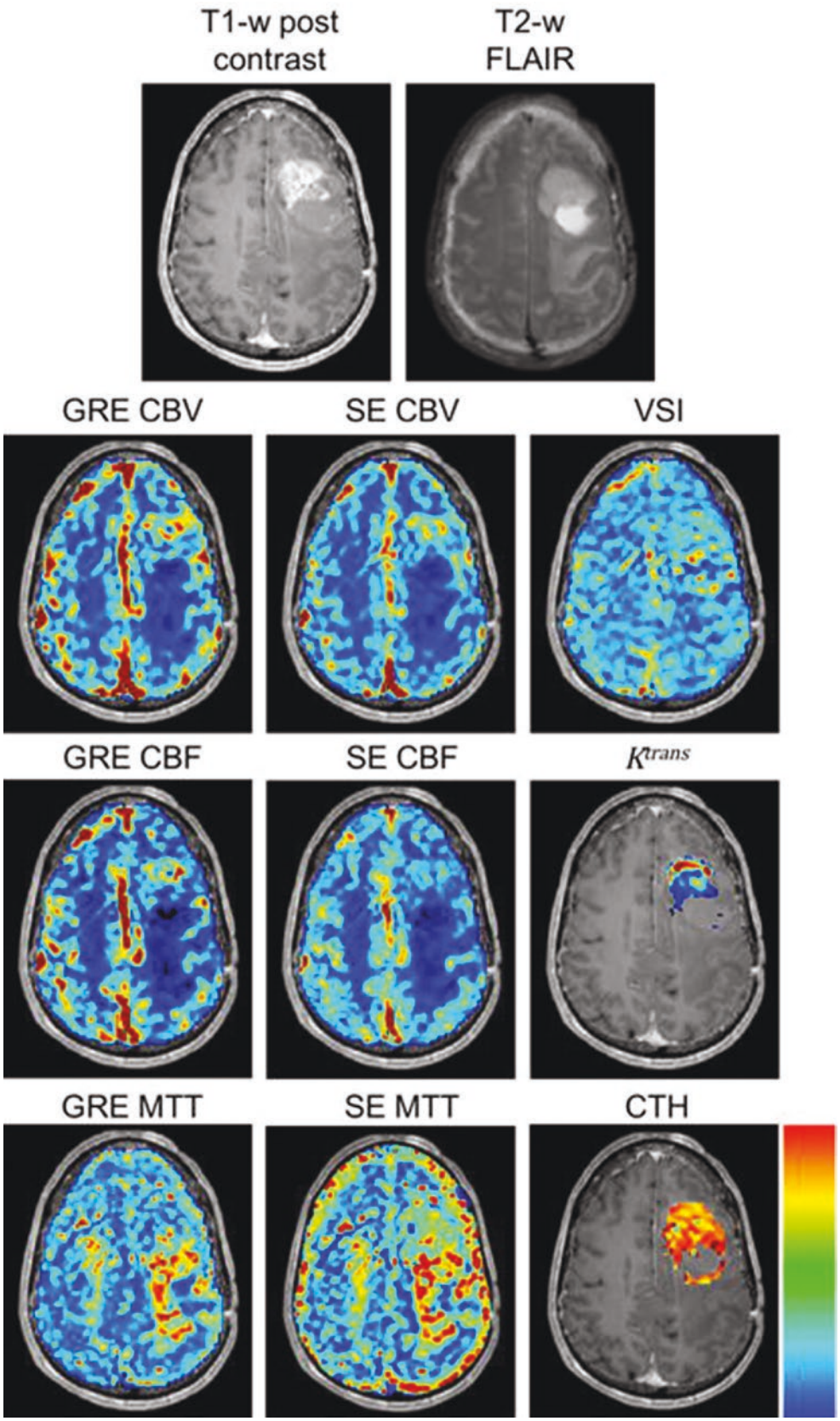

Fig. 2.4 Example of spin and gradient echo (SAGE)-based DSC-MRI maps in a glioblastoma patient showing post-contrast T1-weighted and fluid-attenuated inversion recovery (FLAIR). As would be expected, the tumor CBV, CBF, MTT, and VSI values are higher than those found in contralateral normal-appearing white matter (NAWM). Also note the differences between GRE and SE maps within the tumor, particularly for CBF and MTT. The K^{trans} and CTH maps also exhibit regional heterogeneity within the tumor. Such differences highlight the unique and complementary nature of multi-echo SAGE hemodynamic and vascular sensitivity. For clarity, relative parameter maps are shown using the illustrated colorbar. Reprinted with permission from [2]

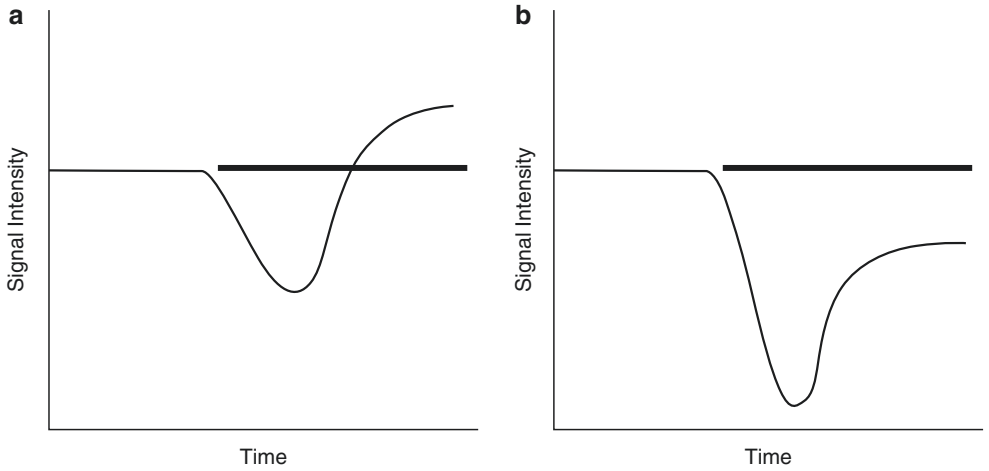

Fig. 2.5 (**a**) Schematic of signal intensity-time curve with BBB leakage and dominant T1 leakage effect. T1-related signal enhancement results in a less signal decrease and subsequent overshooting of the baseline (straight line). This will lead to underestimation of rCBV. (**b**) Schematic of signal intensity-time curve with BBB leakage and dominant T2/T2* effects. T2/T2* effects result in more signal decrease and subsequent undershooting of the baseline (straight line). This will lead to overestimation of rCBV. Reprinted with permission from [50]

The decreased susceptibility differences between the intra- and extravascular compartments due to GBCA leakage result in temporally variant decreases in GBCA T2* relaxivity [25, 103]. More T2* signal decrease can result from mesoscopic magnetic field gradients induced by compartmentalization of GBCA around cells (Fig. 2.6). These changes may be influenced by cellular features such as shape, size, density, polydispersity, and atypia [104]. The potential interaction between T1 and T2/T2* effects in the same lesion further complicates interpretation of rCBV values [105].

There has historically been various methodologies employed to address leakage effects including low flip angle and dual TE acquisitions, preload GBCA dosing, and mathematical post-processing models [105–108]. Current recommendations (see section "Standardization Efforts and Variability of DSC-MRI" below) to correct for leakage effects in single-echo GRE-EPI sequences are to use 60° FA acquisition with full-dose preload or 30° FA without preload, both with full-dose bolus GBCA administration and application of the Boxerman-Schmainda-Weisskoff (BSW) model-based leakage correction method [51, 70, 109–111]. The BSW model generates rCBV corrected for T1 and T2* leakage effects by using linear fitting to calculate voxel-wise differences in ΔR_2^* curves from non-enhancing regions and assumes unidirectional GBCA extravasation [105, 112]. Recent work in a rat glioma model suggests that dual-echo DSC-MRI acquisitions along with a combined biophysical and pharmacokinetic method can potentially eliminate the need for preload GBCA dosing [113].

Superparamagnetic contrast agents such as iron oxide nanoparticles are a newer type of contrast agent that may be advantageous compared to GBCAs given their lack of extravasation, more prominent T2 and T2* relaxivity, and recent concerns about potential long-term effects of gadolinium tissue deposition [114]. Though there are no current such blood pool agents approved for DSC-MRI, ferumoxytol can be used off-label for DSC-MRI [115]. Ferumoxytol is a macromolecular, carbohydrate-coated iron oxide particle that has been sold under the name Feraheme as an iron replacement for adult renal failure patients [116, 117], and several studies have shown promise of DSC-MRI using this agent to distinguish pseudoprogression from tumor progression in brain tumor patients [118, 119].

Standardization Efforts and Variability of DSC-MRI

As with DCE-MRI, there has been a lack of standardized methodology for DSC-MRI [120]. Significant variation in rCBV values can result from differences in image acquisition and post-processing methods, particularly with regard to dealing with leakage effects [121]. This lack of standardization has made inclusion of DSC-MRI into clinical trials and routine practice rather difficult, and to help address this, the American Society of Functional Neuroradiology (ASFNR) published its recommended DSC-MRI protocol in 2015 centered around 1/4–full-dose preload GBCA administration, an intermediate (60°) flip angle, field strength-dependent TE,

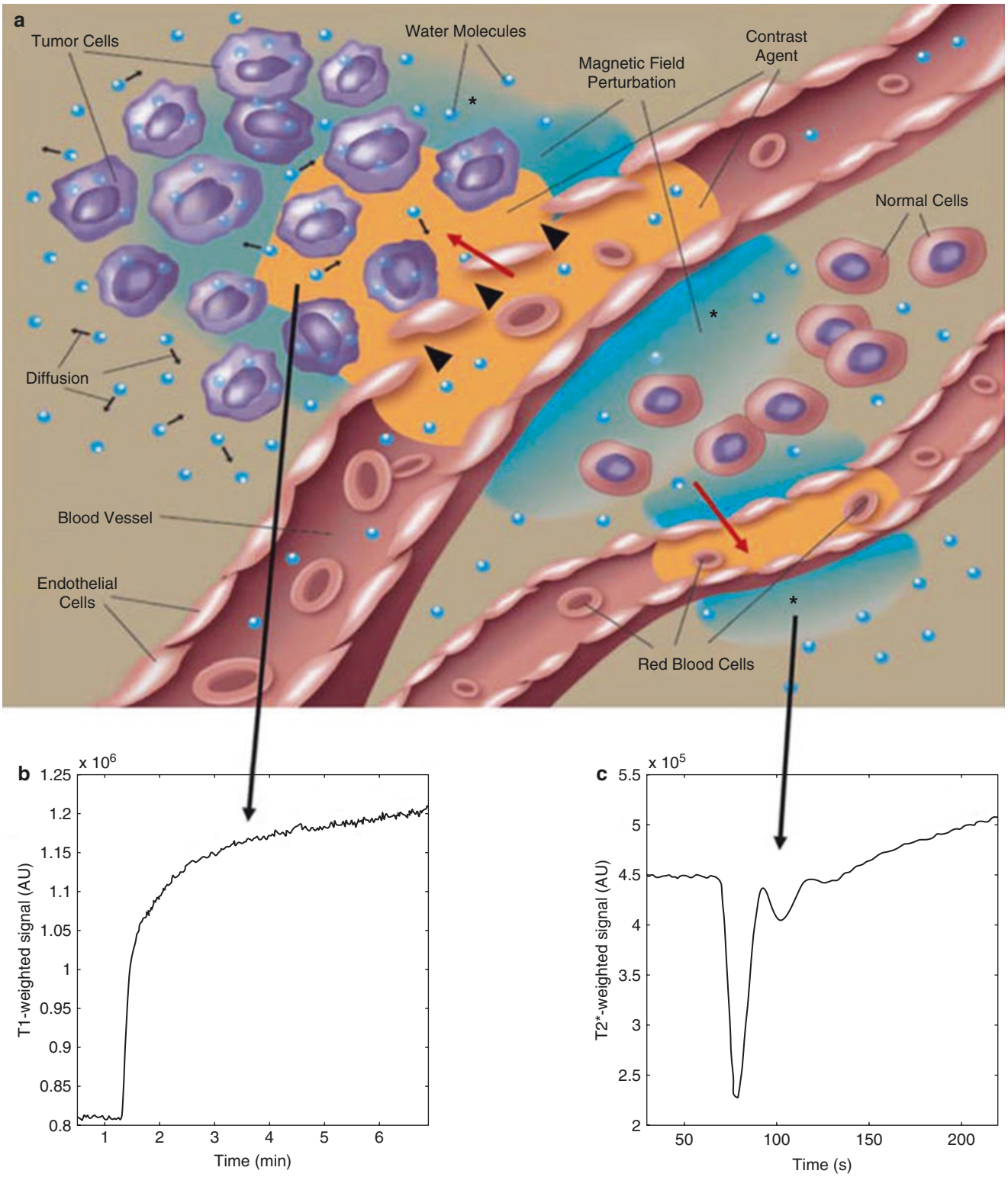

Fig. 2.6 Illustration of contrast administration (CA) distribution within tissue, its interaction with water protons (**a**), and the induced T1-weighted (**b**) or T2*-weighted (**c**) signal changes. When the blood–brain barrier is intact, as illustrated in the lower blood vessel, the CA only has direct access to intravascular water (red arrow) so that the associated change in the effective tissue T1 is small. However, if the blood–brain barrier is disrupted (top blood vessel, black triangles) the CA distribution and microscopic interaction with water within the extravascular space (red arrow) substantially decreases tissue T1 and increases a T1-weighted signal (**b**), like that used for DCE-MRI. The compartmentalization of CA in blood (lower blood vessel) or in the extravascular extracellular space (top blood vessel) gives rise to mesoscopic magnetic field gradients surrounding these compartments (as denoted by the asterisks). The diffusion of water through these fields (small black arrows) decreases T2* and a T2*-weighted signal like that used for DSC-MRI. Reprinted with permission from [2]

and model-based leakage correction (Table 2.3). The Brain Tumor Imaging Protocol (BTIP) consensus recommendations [122], also published in 2015, stipulate that conventional contrast-enhanced T1-weighted imaging be acquired following single-dose GBCA administration, thereby impacting the design of a protocol that incorporates DSC-MRI. To maintain BTIP compatibility, either single-dose GBCA must be split between preload and DSC-MRI bolus before conventional post-contrast imaging, or a full-dose preload must precede post-contrast imaging, followed by variable-dose DSC-MRI bolus. In 2018, Schmainda et al. [123] performed a multicenter DSC-MRI study composed of low-grade and high-grade gliomas. These scans were obtained with a GRE-EPI sequence with preload at a single institution and then seven sites used a variety of model-based post-processing leakage correction, including no correction at all, to compute DSC-MRI metrics. These multicenter results confirmed other prior studies showing the advantages of using preload and model-based leakage correction to obtain consistent results across institutions and distinguish low- from high-grade tumors using a common threshold [65, 106, 107, 112, 121].

Recent work by Semmineh et al. [70] found that by using a population-based digital reference object (DRO) simulating a glioblastoma and the ASFNR recommendations of TE = 30 ms and 60° FA at 1.5 T and 3 T resulted in outstanding precision and accuracy for single-dose preload and single-dose DSC bolus ("1+1" dosing scheme). However, notably worse results were found using fractional GBCA doses, particularly those without preload dosing and at 1.5 T. They also found that a protocol using no-preload dose, a low (30°) FA, and TE = 30 ms at 3 T performed essentially as well as the 1+1 dosing scheme, and in 2019, Schmainda et al. published clinical validation of those DRO results in a four-institution study (Fig. 2.7) [71]. This low-FA, no-preload methodology could be a preferred standardized DSC-MRI methodology because it is a simpler technique with fewer injections and less volume of GBCA. Further multicenter validation, particularly at 1.5 T, is needed.

Again, as with DCE-MRI, there is little data regarding the repeatability of DSC-MRI. Recently, Prah et al. compared repeatability of six common post-processing methods to estimate normalized rCBV (nrCBV) and standardized rCBV (srCBV) [101]. They performed double-baseline examinations in 33 patients with newly diagnosed untreated glioblastoma. Repeat MRI examinations were obtained within eight days. Those methods that used post-processing leakage correction of $\Delta(\text{Delta})R_2^*(t)$ resulted in superior repeatability and compared to nrCBV, srCBV had less variability and needed fewer participants to detect a 10% or 20% change (Fig. 2.8).

To address the lack of standardization of DSC-MRI, QIBA has recently initiated the DSC-MRI Biomarker Committee whose goal is to standardize DSC-MRI methods [124].

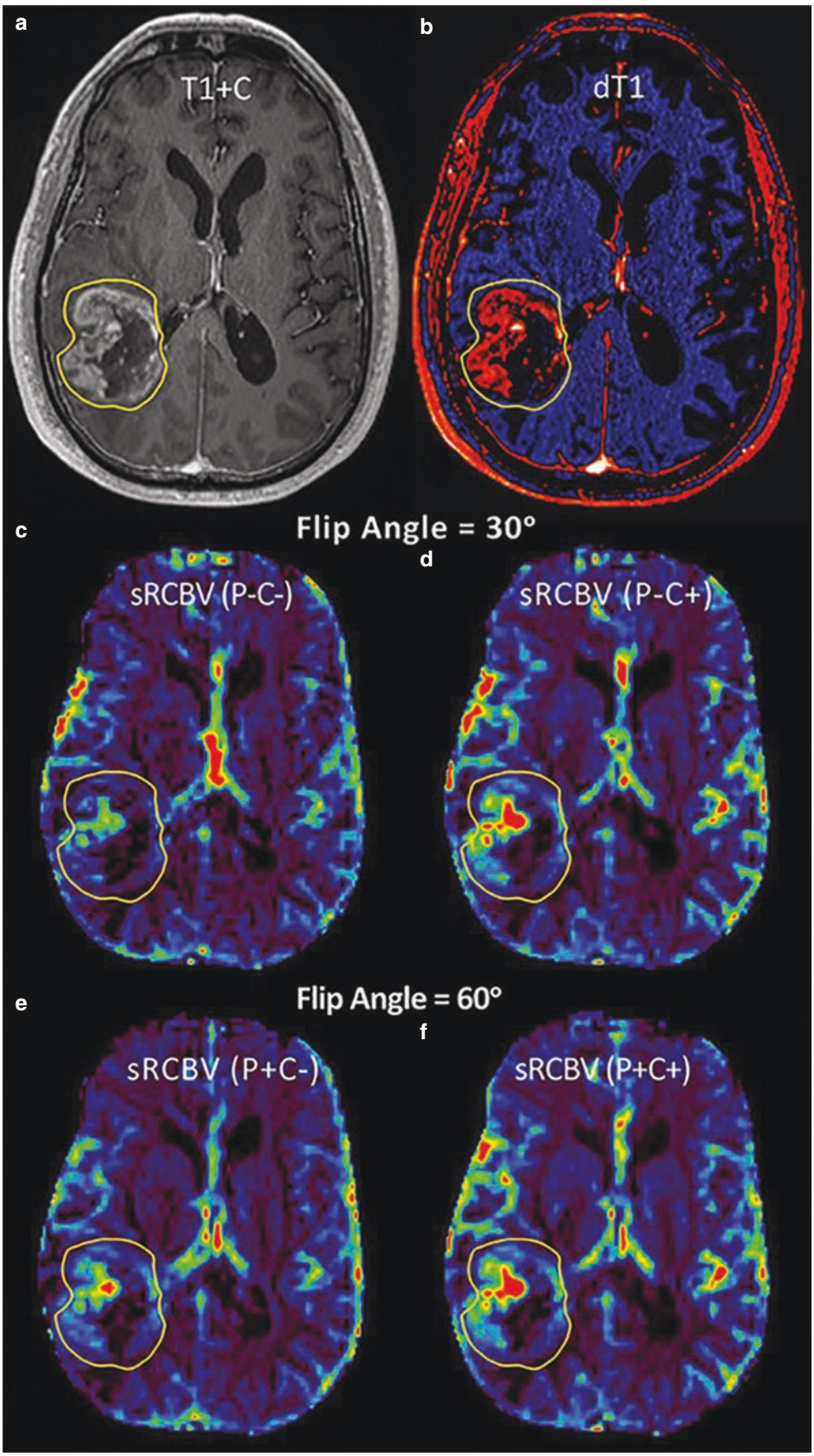

Fig. 2.7 Images and standardized rCBV (srCBV) parameter maps from a patient with glioblastoma. Shown are the post-contrast T1-weighted (T1 + C) (**a**) and quantitative delta T1 (dT1) maps computed from the difference between calibrated and registered pre- and post-contrast T1-weighted images (**b**). Images with the corresponding srCBV maps obtained from the first DSC-MR imaging contrast dose (**c**, **d**) without preload (P−) and without leakage correction (C−) and without preload (P−) plus leakage correction (C+). The srCBVs obtained during the second contrast dose (**e**, **f**) and thus after the preload are shown without (P+/C−) and with (P+/C+) leakage correction. The srCBV maps are qualitatively similar for the 30°/P−/C+ (**d**) and 60°/P+/C+ protocols (**f**). Reprinted from [71]

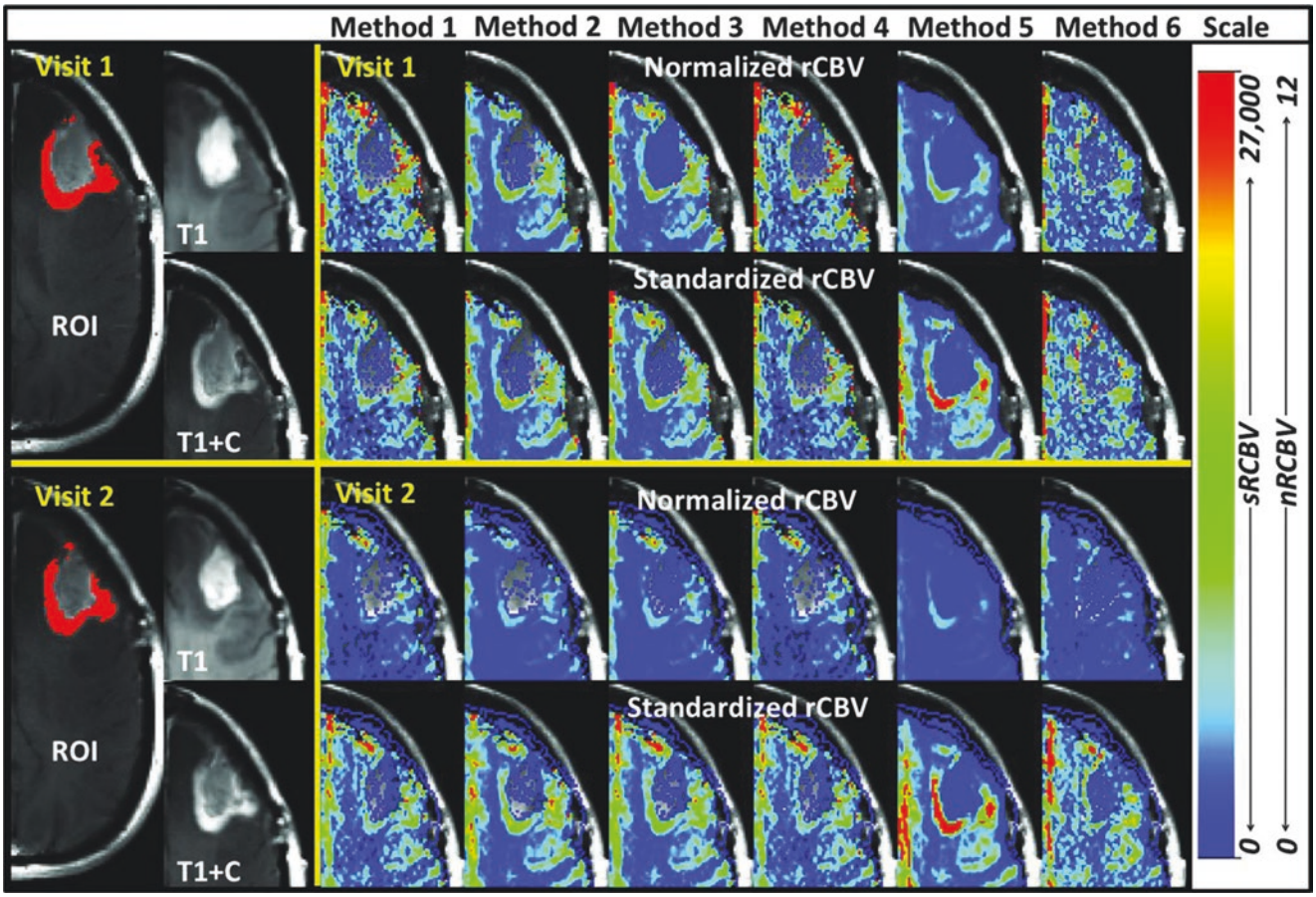

Fig. 2.8 Visual comparison of nrCBV and srCBV. Methods 1–6 (across) for visit 1 (top two rows) and visit 2 (bottom two rows) in the same subject in approximately the same section for visits 1 and 2. These differences in repeatability are especially evident when comparing srCBV method 2 (best repeatability) with srCBV method 5 (worse repeatability) between visits. Method 2 is visually consistent over visits, yet method 5 reveals an extending area of increased rCBV from visit 1 to visit 2. Less repeatable estimation methods could lead to errors in interpretation clinically because the rCBV maps in this figure should appear visually the same in both visits. Clinically, using rCBV methods with greater repeatability should provide clinicians with improved confidence in interpretation by providing a reliable assessment of progression or response to treatment. All data are presented with the same respective scale for nrCBV or srCBV and are in arbitrary units. Reprinted from [101]

Conclusion

In summary, both DCE-MRI and DSC-MRI approaches offer overlapping and complementary insights into the microvasculature and hemodynamics of the brain in health and disease. While both have existed for several decades, routine, standardized clinical implementation remains elusive. A recent 2017 systematic review and meta-analysis by Patel et al. [120] found that while individual studies of DCE-MRI and DSC-MRI appear to have good accuracy for differentiating viable glioma from post-treatment changes, the reported thresholds have significant variability. This highlights the great promise of these techniques beyond conventional MRI for important clinical applications, but emphasizes the need to standardize technique and demonstrate acceptable variability of these methods. A table of key literature of DCE-MRI and DSC-MRI covered in this chapter is listed in Table 2.4.

Table 2.4 Key literature

Authors	Article title	Significance
Tofts and Kermode	Measurement of the blood-brain barrier permeability and leakage space using dynamic MR imaging. 1. Fundamental concepts. Magn Reson Med. 1991;17:357–67	Landmark article on the application of DCE-MRI in the brain
Tofts et al.	Estimating kinetic parameters from dynamic contrast-enhanced T1-weighted MRI of a diffusable tracer: standardized quantities and symbols. J Magn Reson Imaging. 1999;10(3):223–32	Important review that provides standardized nomenclature and definitions used in DCE-MRI
Jackson et al.	Reproducibility of quantitative dynamic contrast-enhanced MRI in newly presenting glioma. Br J Radiol 2003;76:153–62	One of the few early reproducibility studies performed of DCE-MRI of the brain
Boxerman et al.	Relative cerebral blood volume maps corrected for contrast agent extravasation significantly correlate with glioma tumor grade, whereas uncorrected maps do not. AJNR Am J Neuroradiol. 2006;27(4):859–67	Highly cited paper showing the importance of leakage correction to determine glioma grade using rCBV from DSC-MRI
Welker et al.	ASFNR Recommendations for Clinical Performance of MR Dynamic Susceptibility Contrast Perfusion Imaging of the Brain. AJNR Am J Neuroradiol 2015;36:E41–51	White paper from the American Society of Functional Neuroradiology that provides guidance on standardized procedures for implementing DSC-MRI for clinical neuroimaging
Prah et al.	Repeatability of standardized and normalized relative CBV in patients with newly diagnosed glioblastoma. AJNR Am J Neuroradiol. 2015;36(9):1654–61	One of the few repeatability studies of DSC-MRI that used six common post-processing techniques in glioblastoma patients and found that leakage-corrected rCBV resulted in the best repeatability for both standardized and normalized rCBV; it also found that compared to normalized rCBV, standardized rCBV had better repeatability and needed fewer patients to detect a change in values
Patel et al.	MR perfusion-weighted imaging in the evaluation of high-grade gliomas after treatment: a systematic review and meta-analysis. Neuro Oncol. 2017;19(1):118–127	A recent systematic review and meta-analysis that found that while individual DCE-MRI and DSC-MRI studies have found good accuracy in differentiating viable glioma tumor from treatment changes, there was significant variability in reported thresholds, and that this highlights the need for standardization of technique
Schmainda et al.	Multisite concordance of DSC-MRI analysis for brain tumors: results of a National Cancer Institute Quantitative Imaging Network collaborative project. AJNR Am J Neuroradiol. 2018;39(6):1008–16	Multi-institution study showing the potential of DSC-MRI to provide consistent results across sites to differentiate low- from high-grade tumors using a common threshold
Barboriak et al.	Interreader variability of dynamic contrast-enhanced MRI of recurrent glioblastoma: the multicenter ACRIN 6677/RTOG 0625 study. Radiology. 2019;290(2):467–76	Recent study in the context of an imaging clinical trial showing that disagreement in reader tumor segmentations can result in significant inter-reader variability of DCE-MRI metrics
Shukla-Dave et al.	Quantitative imaging biomarkers alliance (QIBA) recommendations for improved precision of DWI and DCE-MRI derived biomarkers in multicenter oncology trials. J Magn Reson Imaging. 2019;49(7):e101–21	Evidence-based summary of recommendations to decrease variability of diffusion-weighted imaging (DWI) and DCE-MRI imaging biomarkers from the Radiological Society of North America's (RSNA) Quantitative Imaging Biomarkers Alliance (QIBA)
Quarles et al.	Imaging vascular and hemodynamic features of the brain using dynamic susceptibility contrast and dynamic contrast enhanced MRI. Neuroimage. 2019;187:32–55	Recent comprehensive review of both physical basis and clinical application of DCE- and DSC-MRI
Schmainda et al.	Moving toward a consensus DSC-MRI protocol: validation of a low-flip angle single-dose option as a reference standard for brain tumors. AJNR Am J Neuroradiol. 2019;40(4):626–33	Recent clinical study showing potential of low-flip angle DSC-MRI acquisition without preload GBCA dosing for brain tumor evaluation

DCE-MRI dynamic contrast-enhanced magnetic resonance imaging, *DSC-MRI* dynamic susceptibility contrast magnetic resonance imaging, *GBCA* gadolinium-based contrast agent, *rCBV* relative cerebral blood volume

References

1. Sourbron SP, Buckley DL. Classic models for dynamic contrast-enhanced MRI. NMR Biomed. 2013;26(8):1004–27.
2. Quarles CC, Bell LC, Stokes AM. Imaging vascular and hemodynamic features of the brain using dynamic susceptibility contrast and dynamic contrast enhanced MRI. NeuroImage. 2019;187:32–55.
3. Jahng G-H, Li K-L, Ostergaard L, Calamante F. Perfusion magnetic resonance imaging: a comprehensive update on principles and techniques. Korean J Radiol. 2014;15(5):554–77.
4. Georgiou L, Buckley DL. T1-weighted DCE MRI. In: Cercignani M, Dowell NG, Tofts P, editors. Quantitative MRI of the brain: principles of physical measurement. 2nd ed. Boca Raton: CRC Press; 2018. p. 251–68.
5. Shukla-Dave A, Obuchowski NA, Chenevert TL, Jambawalikar S, Schwartz LH, Malyarenko D, et al. Quantitative imaging biomarkers alliance (QIBA) recommendations for improved precision of DWI and DCE-MRI derived biomarkers in multicenter oncology trials. J Magn Reson Imaging. 2018;49(7):101–21.
6. Tofts PS, Brix G, Buckley DL, Evelhoch JL, Henderson E, Knopp MV, et al. Estimating kinetic parameters from dynamic contrast-enhanced t1-weighted MRI of a diffusable tracer: standardized quantities and symbols. J Magn Reson Imaging. 1999;10(3):223–32.
7. O'Connor JP, Aboagye EO, Adams JE, et al. Imaging biomarker road-map for cancer studies. Nat Rev Clin Oncol. 2017;14(3):169–86.
8. Tofts PS. Modeling tracer kinetics in dynamic Gd-DTPA MR imaging. J Magn Reson Imaging. 1997;7(1):91–101.
9. Yoon H, Park S-H, Ye JC. Improved volumetric imaging for DCE-MRI using parallel imaging and dynamic compressed sensing. IEEE Glob Conf. 2014;2014:483–6.
10. Espagnet MR, Bangiyev L, Haber M, Block K, Babb J, Ruggiero V, et al. High-resolution DCE-MRI of the pituitary gland using radial k-space acquisition with compressed sensing reconstruction. Am J Neuroradiol. 2015;36(8):1444–9.
11. Guo Y, Lebel RM, Zhu Y, Lingala SG, Shiroishi MS, Law M, et al. High-resolution whole-brain DCE-MRI using constrained reconstruction: prospective clinical evaluation in brain tumor patients. Med Phys. 2016;43(5):2013–23.
12. Zhao J, Yang Z-Y, Luo B-N, Yang J-Y, Chu J-P. Quantitative evaluation of diffusion and dynamic contrast-enhanced MR in tumor parenchyma and peritumoral area for distinction of brain tumors. PLoS One. 2015;10(9):e0138573.
13. Abe T, Mizobuchi Y, Nakajima K, Otomi Y, Irahara S, Obama Y, et al. Diagnosis of brain tumors using dynamic contrast-enhanced perfusion imaging with a short acquisition time. Springerplus. 2015;4(1):88.
14. Haacke EM, Filleti CL, Gattu R, Ciulla C, Al-Bashir A, Suryanarayanan K, et al. New algorithm for quantifying vascular changes in dynamic contrast-enhanced MRI independent of absoluteT1 values. Magn Reson Med. 2007;58(3):463–72.
15. Tietze A, Mouridsen K, Mikkelsen IK. The impact of reliable prebolus T 1 measurements or a fixed T1 value in the assessment of glioma patients with dynamic contrast enhancing MRI. Neuroradiology. 2015;57(6):561–72.
16. Fennessy FM, Fedorov A, Gupta SN, Schmidt EJ, Tempany CM, Mulkern RV. Practical considerations in T1 mapping of prostate for dynamic contrast enhancement pharmacokinetic analyses. Magn Reson Imaging. 2012;30(9):1224–33.
17. Besa C, Bane O, Jajamovich G, Marchione J, Taouli B. 3D T1 relaxometry pre and post gadoxetic acid injection for the assessment of liver cirrhosis and liver function. Magn Reson Imaging. 2015;33(9):1075–82.
18. Kim KA, Park M-S, Kim I-S, Kiefer B, Chung W-S, Kim M-J, et al. Quantitative evaluation of liver cirrhosis using T1 relaxation time with 3 tesla MRI before and after oxygen inhalation. J Magn Reson Imaging. 2012;36(2):405–10.
19. Stikov N, Boudreau M, Levesque IR, Tardif CL, Barral JK, Pike GB. On the accuracy of T1mapping: Searching for common ground. Magn Reson Med. 2015;73(3):514–22.
20. Barker GJ, Simmons A, Arridge SR, Tofts PS. A simple method for investigating the effects of non-uniformity of radiofrequency transmission and radiofrequency reception in MRI. Br J Radiol. 1998;71(841):59–67.
21. Parker GJ, Barker GJ, Tofts PS. Accurate multislice gradient echoT1 measurement in the presence of non-ideal RF pulse shape and RF field nonuniformity. Magn Reson Med. 2001;45(5):838–45.
22. Dowell NG, Tofts PS. Fast, accurate, and precise mapping of the RF field in vivo using the 180° signal null. Magn Reson Med. 2007;58(3):622–30.
23. Larsson HBW, Courivaud F, Rostrup E, Hansen AE. Measurement of brain perfusion, blood volume, and blood-brain barrier permeability, using dynamic contrast-enhancedT1-weighted MRI at 3 tesla. Magn Reson Med. 2009;62(5):1270–81.
24. Hansen AE, Pedersen H, Rostrup E, Larsson HB. Partial volume effect (PVE) on the arterial input function (AIF) inT1-weighted perfusion imaging and limitations of the multiplicative rescaling approach. Magn Reson Med. 2009;62(4):1055–9.
25. Sourbron S, Ingrisch M, Siefert A, Resier M, Herrmann K. Quantification of cerebral blood flow, cerebral blood volume, and blood-brain-barrier leakage with DCE-MRI. Magn Reson Med. 2009;62(1):205–17.
26. Buckley DL, Roberts C, Parker GJM, Logue JP, Hutchinson CE. Prostate cancer: evaluation of vascular characteristics with dynamic contrast-enhanced T1-weighted MR imaging—initial experience. Radiology. 2004;233(3):709–15.
27. Quarles CC, Gore JC, Xu L, Yankeelov TE. Comparison of dual-echo DSC-MRI- and DCE-MRI-derived contrast agent kinetic parameters. Magn Reson Imaging. 2012;30(7):944–53.
28. Narang J, Jain R, Arbab AS, Mikkelsen T, Scarpace L, Rosenblum ML, et al. Differentiating treatment-induced necrosis from recurrent/progressive brain tumor using non-model-based semiquantitative indices derived from dynamic contrast-enhanced T1-weighted MR perfusion. Neuro-Oncology. 2011;13(9):1037–46.
29. Parker GJM, Buckley DL. Tracer kinetic modeling for T1-weighted DCE-MRI. In: Jackson A, Buckley DL, Parker GJM, editors. Dynamic contrast-enhanced MRI in oncology. Berlin: Springer; 2005. p. 81–92.
30. Paldino MJ, Barboriak DP. Fundamentals of quantitative dynamic contrast-enhanced MR imaging. Magn Reson Imaging Clin N Am. 2009;17(2):277–89.
31. Gribbestad IS, Gjesdal KI, Nilsen G, Lundgren S, Hjelstuen MHB, Jackson A. An introduction to dynamic contrast-enhanced MRI in oncology. In: Jackson A, Buckley DL, Parker GJM, editors. Dynamic contrast-enhanced magnetic resonance imaging in oncology. Berlin: Springer; 2005. p. 81–92.
32. Padhani AR. Dynamic contrast-enhanced MRI in clinical oncology: current status and future directions. J Magn Reson Imaging. 2002;16(4):407–22.
33. Tofts PS, Kermode AG. Measurement of the blood-brain barrier permeability and leakage space using dynamic MR imaging. 1. Fundamental concepts. Magn Reson Med. 1991;17(2):357–67.
34. Gerstner ER, Sorensen AG, Jain RK, Batchelor TT. Advances in neuroimaging techniques for the evaluation of tumor growth, vascular permeability, and angiogenesis in gliomas. Curr Opin Neurol. 2008;21(6):728–35.

35. Zaharchuk G. Theoretical basis of hemodynamic MR imaging techniques to measure cerebral blood volume, cerebral blood flow, and permeability. AJNR Am J Neuroradiol. 2007;28(10):1850–8.
36. Brix G, Bahner ML, Hoffmann U, Horvath A, Schreiber W. Regional blood flow, capillary permeability, and compartmental volumes: measurement with dynamic CT–initial experience. Radiology. 1999;210(1):269–76.
37. Patlak CS, Blasberg RG, Fenstermacher JD. Graphical evaluation of blood-to-brain transfer constants from multiple-time uptake data. J Cereb Blood Flow Metab. 1983;3(1):1–7.
38. Brix G, Kiessling F, Lucht R, Darai S, Wasser K, Delorme S, Griebel J. Microcirculation and microvasculature in breast tumors: pharmacokinetic analysis of dynamic MR image series. Magn Reson Med. 2004;52(2):420–9.
39. Sourbron SP, Buckley DL. Tracer kinetic modeling in MRI: estimating perfusion and capillary permeability. Phys Med Biol. 2012;57(2):R1–R33.
40. Naish JH, Kershaw LE, Buckley DL, et al. Modeling of contrast agent kinetics in the lung using T1-weighted dynamic contrast-enhanced MRI. Magn Reson Med. 2009;61(6):1507–14.
41. Brix G, Zwick S, Kiessling F, Griebel J. Pharmacokinetic analysis of tissue microcirculation using nested models: multimodel interference and parameter identifiability. Med Phys. 2009;36(7):2923–33.
42. Quantitative Imaging Biomarkers Alliance. Rsna.org. 2019. Available from: https://www.rsna.org/en/research/quantitative-imaging-biomarkers-alliance.
43. Profiles. Profiles - QIBA Wiki. 2019. Available from https://qibawiki.rsna.org/index.php/Profiles.
44. Bane O, Hectors SJ, Wagner M, Arlinghaus LL, Aryal MP, Cao Y, et al. Accuracy, repeatability, and interplatform reproducibility of T1 quantification methods used for DCE-MRI: Results from a multicenter phantom study. Magn Reson Med. 2018;79(5):2564–75.
45. Quantitative Imaging Data Warehouse (QIDW). 2019. Available from: https://www.rsna.org/en/research/quantitative-imaging-biomarkers-alliance/quantitative-imaging-data-warehouse.
46. Bliesener Y, Zhong X, Guo Y, Boss M, Bosca R, Laue H, et al. Radiofrequency transmit calibration: a multi-center evaluation of vendor-provided radiofrequency transmit mapping methods. Med Phys. 2019;46(6):2629–37.
47. Kim H, Mousa M, Schexnailder P, Hergenrother R, Bolding M, Ntsikoussalabongui B, et al. Portable perfusion phantom for quantitative DCE-MRI of the abdomen. Med Phys. 2017;44(10):5198–209.
48. Jackson A, Jayson GC, Li KL, Zhu XP, Checkley DR, Tessier JJL, et al. Reproducibility of quantitative dynamic contrast-enhanced MRI in newly presenting glioma. Br J Radiol. 2003;76(903):153–62.
49. Barboriak DP, Zhang Z, Desai P, Snyder BS, Safriel Y, Mckinstry RC, et al. Interreader variability of dynamic contrast-enhanced MRI of recurrent glioblastoma: the multicenter ACRIN 6677/RTOG 0625 study. Radiology. 2019;290(2):467–76.
50. Shiroishi MS, Castellazzi G, Boxerman JL, Damore F, Essig M, Nguyen TB, et al. Principles of T2*-weighted dynamic susceptibility contrast MRI technique in brain tumor imaging. J Magn Reson Imaging. 2014;41(2):296–313.
51. Welker K, Boxerman J, Kalnin A, Kaufmann T, Shiroishi M, Wintermark M. ASFNR recommendations for clinical performance of MR dynamic susceptibility contrast perfusion imaging of the brain. Am J Neuroradiol. 2015;36(6):E41–51.
52. Jonathan SV, Vakil P, Jeong Y, Ansari S, Hurley M, Bendok B, Carroll TJ. A radial 3D GRE-EPI pulse sequence with kz blip encoding for whole-brain isotropic 3D perfusion using DSC-MRI bolus tracking with sliding window reconstruction (3D RAZIR). In: Proceedings of the 21st annual meeting of ISMRM. Salt Lake City, UT, USA. 2013, p 582.
53. Paulson ES, Prah DE, Schmainda KM. Spiral perfusion imaging with consecutive echoes (SPICE) for the simultaneous mapping of DSC- and DCE-MRI parameters in brain tumor patients: theory and initial feasibility. Tomography. 2016;2(4):295–307.
54. Gelderen P, van Grandin C, Petrella JR, Moonen CTW. Rapid three-dimensional MR imaging method for tracking a bolus of contrast agent through the brain. Radiology. 2000;216(2):603–8.
55. Newbould RD, Skare ST, Jochimsen TH, Alley MT, Moseley ME, Albers GW, Bammer R. Perfusion mapping with multiecho multishot parallel imaging EPI. Magn Reson Med. 2007;58(1):70–81.
56. Boxerman JL, Hamberg LM, Rosen BR, Weisskoff RM. MR contrast due to intravascular magnetic susceptibility perturbations. Magn Reson Med. 1995;34(4):555–66.
57. Aronen HJ, Gazit IE, Louis DN, Buchbinder BR, Pardo FS, Weisskoff RM, et al. Cerebral blood volume maps of gliomas: comparison with tumor grade and histologic findings. Radiology. 1994;191(1):41–51.
58. Aronen HJ, Perkio J. Dynamic susceptibility contrast MRI of gliomas. Neuroimaging Clin N Am. 2002;12(4):501–23.
59. Østergaard L, Johannsen P, Høst-Poulsen P, Vestergaard-Poulsen P, Asboe H, Gee AD, Hansen SB, Cold GE, Gjedde A, Gyldensted C. Cerebral blood flow measurements by magnetic resonance imaging bolus tracking: comparison with [15O]H2O positron emission tomography in humans. J Cereb Blood Flow Metab. 1998;18(9):935–40.
60. Østergaard L, Smith DF, Vestergaard-Poulsen P, Hansen S, Gee AD, Gjedde A, Gyldensted C. Absolute cerebral blood flow and blood volume measured by magnetic resonance imaging bolus tracking: comparison with positron emission tomography values. J Cereb Blood Flow Metab. 1998;18(4):425–32.
61. Schmiedeskamp H, Andre JB, Straka M, Christen T, Nagpal S, Recht L, Thomas RP, Zaharchuk G, Bammer R. Simultaneous perfusion and permeability measurements using combined spin- and gradient-echo MRI. J Cereb Blood Flow Metab. 2013;33(5):732–43.
62. Schmiedeskamp H, Straka M, Newbould RD, Zaharchuk G, Andre JB, Olivot JM, Moseley ME, Albers GW, Bammer R. Combined spin- and gradient-echo perfusion-weighted imaging. Magn Reson Med. 2012;68(1):30–40.
63. Skinner JT, Robison RK, Elder CP, Newton AT, Damon BM, Quarles CC. Evaluation of a multiple spin- and gradient-echo (SAGE) EPI acquisition with SENSE acceleration: applications for perfusion imaging in and outside the brain. Magn Reson Imaging. 2014;32(10):1171–80.
64. Stokes AM, Skinner JT, Yankeelov TE, Quarles CC. Assessment of a simplified spin and gradient echo (sSAGE) approach for human brain tumor perfusion imaging. Magn Reson Imaging. 2016;34(9):1248–55.
65. Donahue KM, Krouwer HG, Rand SD, Pathak AP, Marszalkowski CS, Censky SC, et al. Utility of simultaneously acquired gradient-echo and spin-echo cerebral blood volume and morphology maps in brain tumor patients. Magn Reson Med. 2000;43(6):845–53.
66. Calamante F, Willats L, Gadian DG, Connelly A. Bolus delay and dispersion in perfusion MRI: implications for tissue predictor models in stroke. Magn Reson Med. 2006;55(5):1180–5.
67. Jochimsen TH, Newbould RD, Skare ST, Clayton DB, Albers GW, Moseley ME, Bammer R. Identifying systematic errors in quantitative dynamic susceptibility contrast perfusion imaging by high-resolution multi-echo parallel EPI. NMR Biomed. 2007;20(4):429–38.
68. Chakhoyan A, Leu K, Pope W, Cloughesy T, Ellingson B. Improved spatiotemporal resolution of dynamic susceptibility contrast perfusion MRI in brain tumors using simultaneous multislice echo-planar imaging. Am J Neuroradiol. 2017;39(1):43–5.

69. Osch MJV, Vonken E-JP, Wu O, Viergever MA, Grond JVD, Bakker CJ. Model of the human vasculature for studying the influence of contrast injection speed on cerebral perfusion MRI. Magn Reson Med. 2003;50(3):614–22.
70. Semmineh N, Bell L, Stokes A, Hu L, Boxerman J, Quarles C. Optimization of acquisition and analysis methods for clinical dynamic susceptibility contrast MRI Using a population-based digital reference object. Am J Neuroradiol. 2018;39(11):1981–8.
71. Schmainda K, Prah M, Hu L, Quarles C, Semmineh N, Rand S, et al. Moving toward a consensus DSC-MRI protocol: validation of a low–flip angle single-dose option as a reference standard for brain tumors. Am J Neuroradiol. 2019;40(4):626–33.
72. Zierler KL. Circulation times and the theory of indicator-dilution methods for determining blood flow and volume. In: Handbook of physiology. Baltimore: Williams & Wilkins; 1962. p. 585–615.
73. Rosen BR, Belliveau JW, Vevea JM, Brady TJ. Perfusion imaging with NMR contrast agents. Magn Reson Med. 1990;14(2):249–65.
74. Simonsen CZ, Ostergaard L, Vestergaard-Poulsen P, Rohl L, Bjornerud A, Gyldensted C. CBF and CBV measurements by USPIO bolus tracking: reproducibility and comparison with Gd-based values. J Magn Reson Imaging. 1999;9(2):342–7.
75. Kiselev VG. On the theoretical basis of perfusion measurements by dynamic susceptibility contrast MRI. Magn Reson Med. 2001;46(6):1113–22.
76. Calamante F, Connelly A, Van Osch MJP. Nonlinear ΔR2* effects in perfusion quantification using bolus-tracking MRI. Magn Reson Med. 2009;61(2):486–92.
77. Meier P, Zierler KL. On the theory of the indicator-dilution method for measurement of blood flow and volume. J Appl Physiol. 1954;6(12):731–44.
78. Lassen NA. Tracer kinetic methods in medical physiology. New York: Raven Press; 1979.
79. Todd-Pokropek A. Estimating blood flow by deconvolution of the injection of radioisotope tracers. In: Rescigno A, Boicelli A, editors. Cerebral blood flow: mathematical models, instrumentation, and imaging techniques. New York: Plenum Press; 1988. p. 107–19.
80. Rosen BR, Belliveau JW, Chien D. Perfusion imaging by nuclear magnetic resonance. Magn Reson Q. 1989;5(4):263–81.
81. Ostergaard L, Sorensen AG, Kwong KK, Weisskoff RM, Gyldensted C, Rosen BR. High resolution measurement of cerebral blood flow using intravascular tracer bolus passages. Part II: experimental comparison and preliminary results. Magn Reson Med. 1996;36(5):726–36.
82. Wu O, Østergaard L, Weisskoff RM, Benner T, Rosen BR, Sorensen AG. Tracer arrival timing-insensitive technique for estimating flow in MR perfusion- weighted imaging using singular value decomposition with a block-circulant deconvolution matrix. Magn Reson Med. 2003;50(1):164–74.
83. Mouridsen K, Hansen MB, Ostergaard L, Jespersen SN. Reliable estimation of capillary transit time distributions using DSC-MRI. J Cereb Blood Flow Metab. 2014;34(9):1511–21.
84. Troprès I, Grimault S, Vaeth A, Grillon E, Julien C, Payen JF, Lamalle L, Decorps M. Vessel size imaging. Magn Reson Med. 2001;45(3):397–408.
85. Digernes I, Bjørnerud A, Vatnehol SAS, Løvland G, Courivaud F, Vik-Mo E, et al. A theoretical framework for determining cerebral vascular function and heterogeneity from dynamic susceptibility contrast MRI. J Cereb Blood Flow Metab. 2017;37(6):2237–48.
86. Troprès I, Pannetier N, Grand S, Lemasson B, Moisan A, Péoch M, et al. Imaging the microvessel caliber and density: principles and applications of microvascular MRI. Magn Reson Med. 2014;73(1):325–41.
87. Rempp KA, Brix G, Wenz F, Becker CR, Guckel F, Lorenz WJ. Quantification of regional cerebral blood flow and volume with dynamic susceptibility contrast-enhanced MR imaging. Radiology. 1994;193(3):637–41.
88. Calamante F, Morup M, Hansen LK. Defining a local arterial input function for perfusion MRI using independent component analysis. Magn Reson Med. 2004;52(4):789–97.
89. Carroll TJ, Rowley HA, Haughton VM. Automatic calculation of the arterial input function for cerebral perfusion imaging with MR imaging. Radiology. 2003;227(2):593–600.
90. Rausch M, Scheffler K, Rudin M, Radu EW. Analysis of input functions from different arterial branches with gamma variate functions and cluster analysis for quantitative blood volume measurements. Magn Reson Imaging. 2000;18(10):1235–43.
91. Yang C, Karczmar GS, Medved M, Stadler WM. Estimating the arterial input function using two reference tissues in dynamic contrast-enhanced MRI studies: fundamental concepts and simulations. Magn Reson Med. 2004;52(5):1110–7.
92. Gruner R, Bjornara BT, Moen G, Taxt T. Magnetic resonance brain perfusion imaging with voxel-specific arterial input functions. J Magn Reson Imaging. 2006;23(3):273–84.
93. Bjornerud A, Emblem KE. A fully automated method for quantitative cerebral hemodynamic analysis using DSC-MRI. J Cereb Blood Flow Metab. 2010;30(5):1066–78.
94. Huang W, Chen Y, Fedorov A, Li X, Jajamovich GH, Malyarenko DI, Aryal MP, LaViolette PS, Oborski MJ, O'Sullivan F, Abramson RG, Jafari-Khouzani K, Afzal A, Tudorica A, Moloney B, Gupta SN, Besa C, Kalpathy-Cramer J, Mountz JM, Laymon CM, Muzi M, Schmainda K, Cao Y, Chenevert TL, Taouli B, Yankeelov TE, Fennessy F, Li X. The impact of arterial input function determination variations on prostate dynamic contrast-enhanced magnetic resonance imaging pharmacokinetic modeling: a multicenter data analysis challenge. Tomography. 2016;2(1):56–66.
95. Calamante F. Arterial input function in perfusion MRI: a comprehensive review. Prog Nucl Magn Reson Spectrosc. 2013;74:1–32.
96. Willats L, Christensen S, Ma HK, Donnan GA, Connelly A, Calamante F. Validating a local arterial input function method for improved perfusion quantification in stroke. J Cereb Blood Flow Metab. 2011;31(11):2189–98.
97. Nejad-Davarani SP, Bagher-Ebadian H, Ewing JR, Noll DC, Mikkelsen T, Chopp M, Jiang Q. An extended vascular model for less biased estimation of permeability parameters in DCE-T1 images. NMR Biomed. 2017;30:6.
98. Nejad-Davarani SP, Bagher-Ebadian H, Ewing JR, Noll DC, Mikkelsen T, Chopp M, Jiang Q. A parametric model of the brain vascular system for estimation of the arterial input function (AIF) at the tissue level. NMR Biomed. 2017;30:5.
99. Jackson A, O'Connor J, Thompson G, Mills S. Magnetic resonance perfusion imaging in neuro-oncology. Cancer Imaging. 2008;8:186–99.
100. Wetzel SG, Cha S, Johnson G, et al. Relative cerebral blood volume measurements in intracranial mass lesions: interobserver and intraobserver reproducibility study. Radiology. 2002;224(3):797–803.
101. Prah M, Stufflebeam S, Paulson E, Kalpathy-Cramer J, Gerstner E, Batchelor T, et al. Repeatability of standardized and normalized relative CBV in patients with newly diagnosed glioblastoma. Am J Neuroradiol. 2015;36(9):1654–61.
102. Bedekar D, Jensen T, Schmainda KM. Standardization of relative cerebral blood volume (rCBV) image maps for ease of both inter- and intrapatient comparisons. Magn Reson Med. 2010;64(3):907–13.
103. Quarles CC, Gochberg DF, Gore JC, Yankeelov TE. A theoretical framework to model DSC-MRI data acquired in the presence of contrast agent extravasation. Phys Med Biol. 2009;54(19):5749–66.
104. Semmineh NB, Xu J, Skinner JT, Xie J, Li H, Ayers G, et al. Assessing tumor cytoarchitecture using multiecho DSC-MRI

derived measures of the transverse relaxivity at tracer equilibrium (TRATE). Magn Reson Med. 2015;74(3):772–84.
105. Paulson ES, Schmainda KM. Comparison of dynamic susceptibility-weighted contrast-enhanced MR methods: recommendations for measuring relative cerebral blood volume in brain tumors. Radiology. 2008;249(2):601–13.
106. Boxerman JL, Schmainda KM, Weisskoff RM. Relative cerebral blood volume maps corrected for contrast agent extravasation significantly correlate with glioma tumor grade, whereas uncorrected maps do not. AJNR Am J Neuroradiol. 2006;27(4):859–67.
107. Hu L, Baxter L, Pinnaduwage D, Paine T, Karis J, Feuerstein B, et al. Optimized preload leakage-correction methods to improve the diagnostic accuracy of dynamic susceptibility-weighted contrast-enhanced perfusion MR imaging in posttreatment gliomas. Am J Neuroradiol. 2009;31(1):40–8.
108. Hu L, Baxter L, Smith K, Feuerstein B, Karis J, Eschbacher J, Coons S, Nakaji P, Yeh R, Debbins J, Heiserman J. Relative cerebral blood volume values to differentiate high-grade glioma recurrence from posttreatment radiation effect: direct correlation between image-guided tissue histopathology and localized dynamic susceptibility-weighted contrast-enhanced perfusion MR imaging measurements. Am J Neuroradiol. 2008;30(3):552–8.
109. Leu K, Boxerman JL, Cloughesy TF, Lai A, Nghiemphu PL, Liau LM, Pope WB, Ellingson BM. Improved leakage correction for single-echo dynamic susceptibility contrast perfusion MRI estimates of relative cerebral blood volume in high-grade gliomas by accounting for bidirectional contrast agent exchange. Am J Neuroradiol. 2016;37(8):1440–6.
110. Semmineh NB, Stokes AM, Bell LC, Boxerman JL, Quarles CC. A population-based digital reference object (DRO) for optimizing dynamic susceptibility contrast (DSC)-MRI methods for clinical trials. Tomography. 2017;3(1):41–9.
111. Leu K, Boxerman J, Ellingson B. Effects of MRI protocol parameters, preload injection dose, fractionation strategies, and leakage correction algorithms on the fidelity of dynamic-susceptibility contrast MRI estimates of relative cerebral blood volume in gliomas. Am J Neuroradiol. 2016;38(3):478–84.
112. Schmainda KM, Rand SD, Joseph AM, et al. Characterization of a first-pass gradient- echo spin-echo method to predict brain tumor grade and angiogenesis. AJNR Am J Neuroradiol. 2004;25(9):1524–32.
113. Stokes AM, Semmineh N, Quarles CC. Validation of a T1 and T2* leakage correction method based on multiecho dynamic susceptibility contrast MRI using MION as a reference standard. Magn Reson Med. 2016;76(2):613–25.
114. Varallyay CG, Nesbit E, Horvath A, Varallyay P, Fu R, Gahramanov S, et al. Cerebral blood volume mapping with ferumoxytol in dynamic susceptibility contrast perfusion MRI: comparison to standard of care. J Magn Reson Imaging. 2018;48(2):441–8.
115. Vasanawala SS, Nguyen K-L, Hope MD, Bridges MD, Hope TA, Reeder SB, et al. Safety and technique of ferumoxytol administration for MRI. Magn Reson Med. 2016;75(5):2107–11.
116. Neuwelt EA, et al. The potential of ferumoxytol nanoparticle magnetic resonance imaging, perfusion, and angiography in central nervous system malignancy: a pilot study. Neurosurgery. 2007;60(4):601–11.
117. Varallyay CG, Nesbit E, Fu R, Gahramanov S, Moloney B, Earl E, Muldoon LL, Li X, Rooney WD, Neuwelt EA. High-resolution steady-state cerebral blood volume maps in patients with central nervous system neoplasms using ferumoxytol, a superparamagnetic iron oxide nanoparticle. J Cereb Blood Flow Metab. 2013;33(5):780–6.
118. Gahramanov S, Muldoon LL, Varallyay CG, Li X, Kraemer DF, Fu R, Hamilton BE, Rooney WD, Neuwelt EA. Pseudoprogression of glioblastoma after chemo- and radiation therapy: diagnosis by using dynamic susceptibility-weighted contrast-enhanced perfusion MR imaging with ferumoxytol versus gadoteridol and correlation with survival. Radiology. 2013;266(3):842–52.
119. Gahramanov S, Raslan A, Muldoon L, Hamilton B, Rooney W, Varallyay C, et al. Potential for differentiation of pseudoprogression from true tumor progression with dynamic susceptibility-weighted contrast-enhanced magnetic resonance imaging using ferumoxytol vs. gadoteridol: a pilot study. Int J Radiat. 2011;79(2):514–23.
120. Patel P, Baradaran H, Delgado D, Askin G, Christos P, Tsiouris AJ, et al. MR perfusion-weighted imaging in the evaluation of high-grade gliomas after treatment: a systematic review and meta-analysis. Neuro-Oncology. 2017;19(1):118–27.
121. Boxerman JL, Prah D, Paulson E, Machan J, Bedekar D, Schmainda K. The role of preload and leakage correction in gadolinium-based cerebral blood volume estimation determined by comparison with MION as a criterion standard. Am J Neuroradiol. 2012;33(6):1081–7.
122. Ellingson BM, Bendszus M, Boxerman J, Barboriak D, Erickson BJ, Smits M, et al. Consensus recommendations for a standardized brain tumor imaging protocol in clinical trials. Neuro-Oncology. 2015;17(9):1188–98.
123. Schmainda K, Prah M, Rand S, Liu Y, Logan B, Muzi M, et al. Multisite concordance of DSC-MRI analysis for brain tumors: results of a national cancer institute quantitative imaging network collaborative project. Am J Neuroradiol. 2018;39(6):1008–16.
124. DSC MRI Biomarker Ctte. DSC MRI Biomarker Ctte - QIBA Wiki. 2019. Available from https://qibawiki.rsna.org/index.php/DSC_MRI_Biomarker_Ctte